energies

MDPI

Article

Optimisation and Management of Energy Generated by a Multifunctional MFC-Integrated Composite Chassis for Rail Vehicles

Yiding Liu [1], Sijun Du [2], Christopher Micallef [1], Yu Jia [3,4,*], Yu Shi [4,*] and Darren J. Hughes [1,*]

1 Warwick Manufacturing Group, University of Warwick, Coventry CV4 7AL, UK; Yiding.liu@warwick.ac.uk (Y.L.); Christopher.Micallef@warwick.ac.uk (C.M.)
2 Department of Electrical Engineering and Computer Sciences, University of California at Berkeley, Berkeley, CA 94720, USA; sijun@berkeley.edu
3 School of Engineering and Applied Science, Aston University, Birmingham B4 7ET, UK
4 Department of Mechanical Engineering, University of Chester, Chester CH2 4NU, UK
* Correspondence: yu.jia.gb@ieee.org (Y.J.); y.shi@chester.ac.uk (Y.S.); D.hughes@warwick.ac.uk (D.J.H.)

Received: 29 March 2020; Accepted: 21 May 2020; Published: 28 May 2020

Abstract: With the advancing trend towards lighter and faster rail transport, there is an increasing interest in integrating composite and advanced multifunctional materials in order to infuse smart sensing and monitoring, energy harvesting and wireless capabilities within the otherwise purely mechanical rail structures and the infrastructure. This paper presents a holistic multiphysics numerical study, across both mechanical and electrical domains, that describes an innovative technique of harvesting energy from a piezoelectric micro fiber composites (MFC) built-in composite rail chassis structure. Representative environmental vibration data measured from a rail cabin have been critically leveraged here to help predict the actual vibratory and power output behaviour under service. Time domain mean stress distribution data from the Finite Element simulation were used to predict the raw AC voltage output of the MFCs. Conditioned power output was then calculated using circuit simulation of several state-of-the-art power conditioning circuits. A peak instantaneous rectified power of 181.9 mW was obtained when eight-stage Synchronised Switch Harvesting Capacitors (SSHC) from eight embedded MFCs were located. The results showed that the harvested energy could be sufficient to sustain a self-powered structural health monitoring system with wireless communication capabilities. This study serves as a theoretical foundation of scavenging for vibrational power from the ambient state in a rail environment as well as to pointing to design principles to develop regenerative and power neutral smart vehicles.

Keywords: vibration energy harvesting; micro fiber composite; finite element analysis; circuit design and optimization; power conditioning circuit; lightweight rail vehicle

1. Introduction

Rail transport, as a means of transit for passengers and goods in daily life, is now increasingly targeting and transforming towards lightweight, faster speeds and net zero carbon emissions. The current state-of-the-art in the automotive sector suggests using "right material in the right place" to satisfy the stiffness, strength, and crashworthiness certification requirements. This leads to the application of composite materials, such as carbon fiber or glass fiber reinforced polymers, due to their lighter weight and high stiffness-to-weight ratio. Subsequently, particularly in light of the global energy crisis and environment concerns, smart composites with energy harvesting capabilities have developed into an attractive research frontier [1]. Vibrations exists throughout the rail transportation

system, such as the vibration of floor and vehicle chassis, railway train or tracks, etc., and hence it could offer an alternative energy source to compensate for the dissipation of kinetic energy during vehicle vibration and motion [2].

Vibration-based energy harvesting, as one of the most promising research fields, has been established utilising electromagnetic generators [3], piezoelectric generators [4,5], MEMS-scale electrostatic generators [6], triboelectric [7,8] and magnetostrictive effects [9]. Figure 1 illustrates the means of energy harvesting mechanisms and their possible applications in the railway industry, adopted from [10–15]. However, the application of different energy harvesting systems depends on specific requirements, i.e., environmental conditions and physical constraints [16]. Electromagnetic inductions produce energy harvesting by means of permanent magnets, a coil and a resonating cantilever beam; however, magnets also add to the inertial mass [17]. Electrostatic generators require an initial constant polarisation of voltage field or charge. When using electrets to provide the initial charge, the output impedance is often quite high which makes them less suitable as a power supply [17]. The past 5 years have witnessed the remarkable progress of triboelectric nanogenerators (TENG), which have proven to be simple, reliable, cost-effective and efficient means for high-performance vibration energy harvesting for automotive engines and transmission lines [18]. However, the current output of TENG is usually around several hundred microamperes, while the output voltage can easily reach 1000 V owing to the large inner impedance. A general challenge of TENG is its relatively low current compared with its voltage output, which also hinders its development in high-performance vibration energy harvesting. Magnetostrictive material has the ability to produce kinetic energy from magnetic energy through magneto-mechanical coupling and electromagnetic coupling. The major drawbacks of the magentostrictive system are its difficulty in integration with MEMS, and that it can only produce considerable power near system resonance compared to other energy harvesting methods. However, its development in rail seems rare compared to electromagnetic generators. Among them, piezoelectric materials offer great benefit in converting mechanical energy into electric energy due to their relatively high energy density and scalability [16,19]. As conventional piezoelectric ceramics are brittle and easily broken, the macro-fiber composite (MFC) can be used as an energy harvesting device due to its structural flexibility, high efficiency and almost negligible thickness. The MFCs consist of the integration of rectangular piezo ceramic rods sandwiched between layers of adhesive, electrodes and polyimide film. This assembly enables a ready-to-use package applied as a thin, surface-comfortable sheet to various types of structures or embedded in a composite structure. The successfully application of MFC in energy harvesting has been approved by Shi's work investigating their application into an aircraft's wing structure [20], and Yuan's work on a one tenth scale experimental rig of an urban rail vehicle [21].

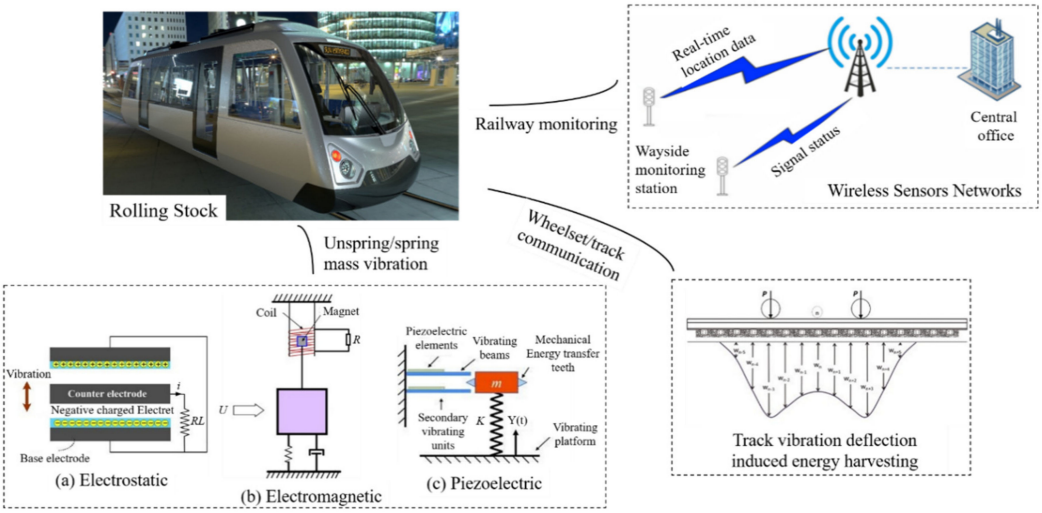

Figure 1. Illustration of energy harvesting applied to the railway industry, adopted from [10–15].

With respect to energy harvesting specific for railway application, most studies have focused on the vehicle brakes, shock absorbers, and exhaust systems and rail/track interfaces. Numerous research endeavours have been extended to investigate the energy harvesting potential from railway tracks as the tracks sustain the full load of the vehicle when the train moves [1]. Zuo et al. [1] stated that the actual harvested power from railway tracks depends on the speed of the train, the weight of the train and the type of railway track. For instance, for a four-wheel railcar of 100 tonnes at a speed of 40 miles/h, the average power potential is about 2 kW under 6.35 mm track deflection according to analytical analysis. This amount of power is sufficient for most of the trackside electric facilities, e.g., the light-emitting diode (LED) signal lights typically require a power of 8–10 W, and level-crossing gates require a power of 150–200 W [1]. Pourghodrat et al. [22] proposed a hydraulic energy harvesting system to harness power from both downward and upward deflections of the track. The system could provide an average power of 1.9 W under a deflection of 2.8 mm and maximum load of 6.4 t. Hadas et al. [23] developed a model-based design of various harvesting systems embedded inside track sleepers and the maximum predicted harvested power was around 2 W when a train was passing at speed.

The works above discussed comparably in large-scale energy harvesting at 1 W to 100 kW, which promised a solution for self-powering the active devices, such as energy recovery from a suspension [2]. However, a fundamental challenge is that such large-scale vibrations are rarely maintained at a time-varying frequency and at alternating velocities, resulting in the energy harvested being unsustainable, inefficient and eventually unreliable for powering functional devices. However, small-scale vibrations are too difficult to avoid during the service of rail vehicles and ideally meeting the energy request under sustainable supplying if they could be efficiently harvested. Hence, the balance of combined vibration control and efficiency of energy harvesting could be a critical concern considered for small-scale vibration harvesting. So far, the most micro-scale harvested power ranging from 10 μW to 100 mW was significantly ignored in the railway industry, especially the vibrations from the vehicle structures when running on the individual routes, and was therefore wasted. However, such energy could be an important source for self-powering the wireless sensors and low-power electronics, which effectively resolves the difficulties of connections by wires/cables during assembly and induced extra weight. The current study focuses on these micro-scale powers harvested from the composite chassis of a rail vehicle under a low frequency operational vibration. Considering the power requirement of sensing and wireless sensor nodes for communication [24], the optimisation and energy management during harvesting process is numerically predicted for the real-world implementations of rail sectors based on our previous works presented in [25,26].

Most existing piezoelectric models are either based on analytical analysis (based on beam theory) [16,27–29] or experimental tests [21–23]. Analytical models are beneficial in understanding the underlying physics; however, it is difficult to simplify the complicated geometries. Experimental evaluations are useful for providing situations that are more realistic; however, they are time and cost consuming and the results are highly subjective due to the possibility of human error. On the other hand, finite element (FE) models can support complex assemblies while including multi-physical modules. Jia and Shi et al. [29] proposed using an FE model to simulate the electrical and mechanical behaviour of an integrated MFC on a carbon fiber composite beam using COMSOL Multiphysics combining solid mechanics, electrostatic and electrical-circuit-physics models. It has a specific requirement on the computer hardware if applied to a large complex geometry, including multi modules.

This work specifically relates to a challenged industrial project at Warwick Manufacturing Group (WMG), the University of Warwick, where a new class of lightweight rail vehicle is in development for upgrading the transportation system of the City of Coventry and lowering the carbon emissions [30]. The vehicle under development follows a "right material in the right place" strategy adopted from the design of automotive vehicles. Figure 2a shows an exploded view of the prototype design of the rail vehicle. The prototype design includes a steel bottom chassis and side module, an aluminium roof structure and composite nose mould to improve the stiffness of the vehicle from a safety perspective. However, in order to further reduce the weight to improve the driving performance and efficiency,

the composite bottom chassis was proposed with an expect of weight saving of 33.5% (from 922.3 kg to 613.5 kg). Moreover, through the optimisation of the efficiency of energy harvesting, composite bottom chassis is also ideal due to a higher stress distribution with the integration of piezoelectric energy harvesters.

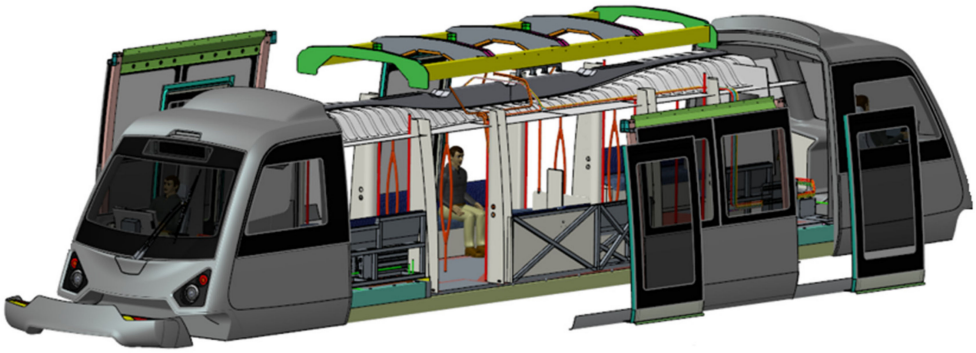

(**a**) Exploded view of the main components in the vehicle

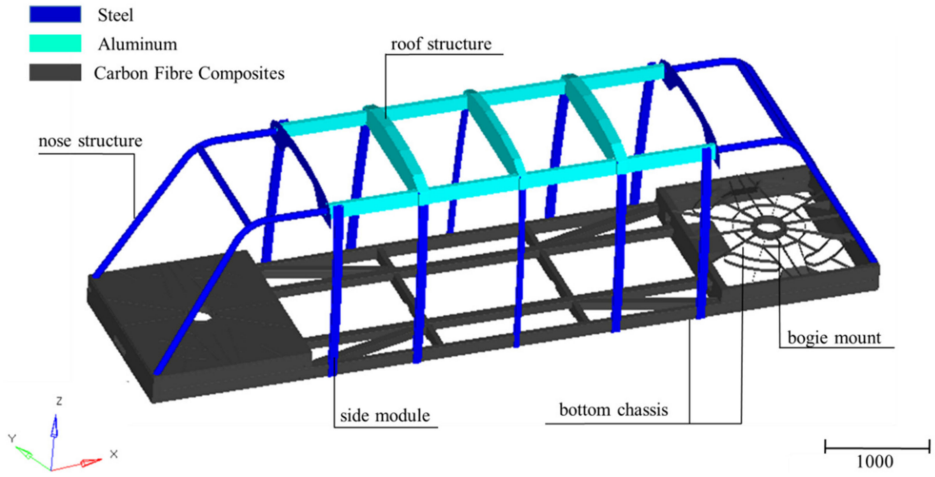

(**b**) Simplified vehicle structure studied in this paper

Figure 2. (**a**) Exploded view of the main components in the rail vehicle; (**b**) multi-material design of a simplified light rail vehicle structure. Units in mm. The vehicle length, width and height are 11.0, 2.7 and 3.1 m, respectively.

To reduce the analysis burden of the complicated vehicle geometry (Figure 2a), beam structures were used to replace the original nose design while the other structures maintained the same, as shown in Figure 2b. Based on that, this paper aimed at harvesting energy from a multifunctional MFC-embedded composite chassis of a simplified rail vehicle structure (Figure 2b), under the representative operational vibration data measured in a rail cabin. The design of the pattern and location of the integrated MFCs within composite chassis was determined by a parametric finite element (FE) study. To meet the actual power demanding of sensors and wireless nodes, the harvested energy was optimised and managed by designing the various rectified circuits strategies. The recoverable rectified power from the chassis vibration was predicted with optimal energy saved compared to other rectification circuit designs. The feasibility of using the harvested energy to sustainably power the smart microsystems was assessed by referring to the power consumptions of such functional components. Figure 3 summarises the schematic of the FE model setup and the power prediction system discussed in this paper.

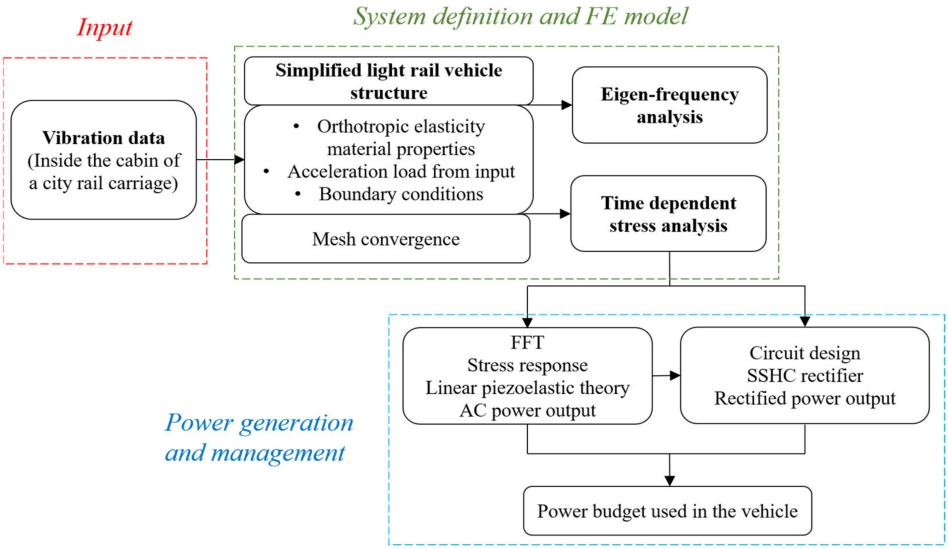

Figure 3. The schematic of the FE model setup and power prediction from the piezoelectric MFC on composite rail chassis when subjected to vibrational data input discussed in this paper.

2. Finite Element Analysis of the Vehicle

2.1. Finite Element Model

For balancing the computing efficiency with a full chassis structure, the symmetric model of the vehicle structure was created using Hypermesh code and OptiStruct solver. A shell model was built by extracting the middle surface from the three-dimensional geometry to save computational cost and time. The entire chassis structure was primarily joined by rigid connections between different structural components. The definition of the boundary conditions of the chassis is illustrated in Figure 4a: the displacement and rotations of the bogie mount central was restricted as the bogie structures are attached to the wheel and stay stable on the track. Multi-point constraint was used to link all the nodes at the middle section to a built independent node and an *x*-symmetric boundary condition was employed. The time-dependent accelerations were input to the built independent node and the deformations were expected to be transferred to the entire chassis. A global element size of 10 mm was confirmed after a parametric study of convergence in the FE solver, as shown in Figure 4b. Therefore, the entire model has a total number of 361,427 shell elements.

The steel and aluminium structural components were modelled using isotropic natures, with the material properties shown in Table 1. The composite bottom chassis was made from RC200T woven fabric CFRP, with the orthotropic material properties obtained from [29] (also shown in Table 1). An Eigenfrequency study of the half chassis structure was firstly performed and the analysis revealed the natural frequency at 6.018 Hz (1st bending mode, see Figure 4c) and 6.763 Hz (1st torsional mode, see Figure 4d), with higher resonant modes summarised in Table 2. A time-dependent transient response analysis was carried out to determine the time-varying dynamic responses of the structure under the given time-dependent acceleration.

Table 1. Properties of the materials used in the vehicle structure. (Material breakdown in Figure 2b).

	Elastic Modulus (GPa)	Poisson's Ratio	Density (kg/m^3)
Steel	210	0.29	7850
Aluminium	69	0.3	2700
CFRP (RC200T) [29]	E_x = 59.45, E_y = 60.30, E_z = 3.90 G_{xy} = 62.90, G_{yz} = 1.50, G_{xz} = 62.35	υ_{xy} = 0.3 υ_{yz} = 0.4 υ_{xz} = 0.3	1800

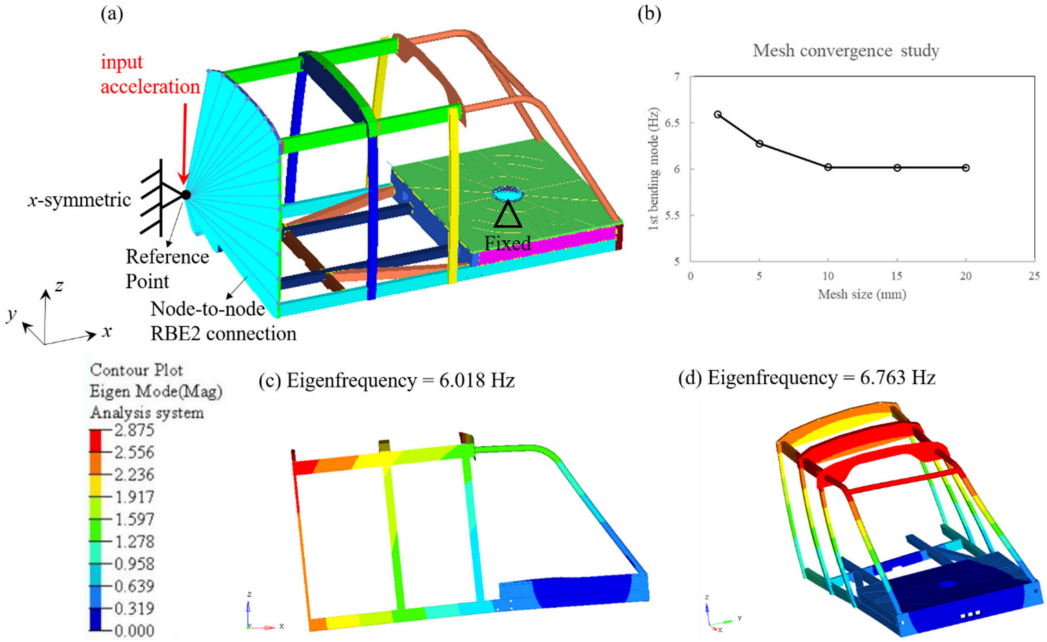

Figure 4. (**a**) Boundary conditions of the FE model of the vehicle, (**b**) mesh convergence study, (**c**) 1st bending mode (6.018 Hz) and (**d**) 1st torsional mode (6.763 Hz) of the vehicle.

Table 2. Comparison of resonant frequencies for various modes of the vehicle.

Mode	Freq. (Hz)
1st bending (Figure 4b)	6.018
2nd bending	19.935
1st torsional (Figure 4c)	6.763
2nd torsional	14.407
3rd torsional	21.921
1st lateral	23.839

2.2. *Vibration Data Analysis*

Vibration data were measured directly from a representative environment inside the cabin of a city rail carriage using 3 axis Gulf Coast Data Concepts (GCDC) MEMS accelerometer data loggers with a sample rate of 400 Hz to 800 Hz [31] and has been published in [29]. The total period of the selected data covers approximately 9 s. The axes were defined as being identical to the coordinates shown in Figure 4a: the *x*-axis is along the vehicle, the *y*-axis is across the vehicle, and the *z*-axis is vertical through the vehicle. The time domain data were processed and analysed using Fast Fourier Transform (FFT) in MATLAB, as shown in Figure 5. *X*-axis vibration (mean amplitude was 0.02126 g) contained an evident frequency peak at 1.53 Hz, followed by minor harmonics. *Y*-axis (mean amplitude was 0.01205 g) was more broadband, with a few harmonics at different frequencies. *Z*-axis vibration (mean amplitude was 0.03007 g) experienced peaks at 1.28 Hz, with a flat active frequency range covering up to 10 Hz. All of the accelerations from the three axes contribute to the movement of the vehicle. It should be noted that the vibration data in the three axes depend on many factors, i.e., the health condition of the vehicle, the track roughness. These acceleration data were used as excitation inputs for the FE model.

It should be noted that the natural frequency of the prototype structure at 6.018 Hz does not match with the first active frequency peak of the three axes vibration data; therefore, the power response was primarily non-resonant for the unmatched case.

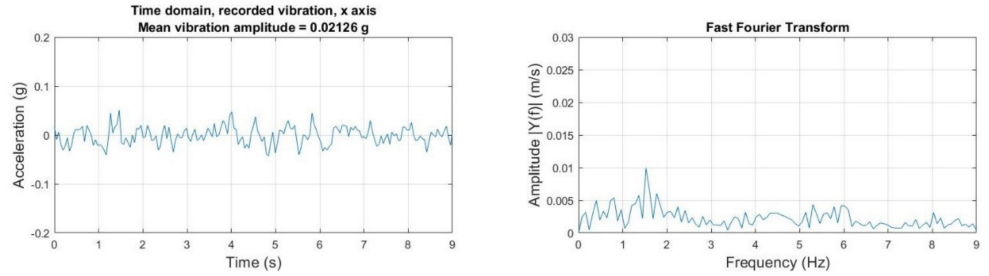

(**a**) *X* axis

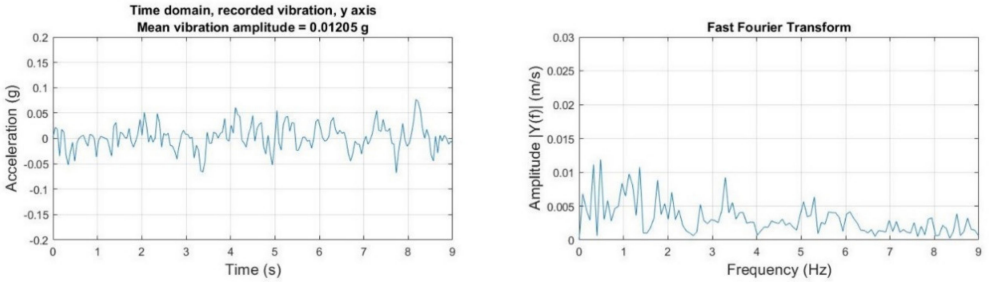

(**b**) *Y* axis

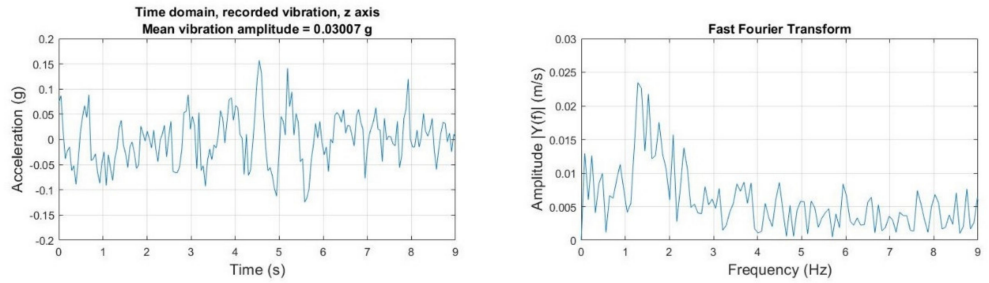

(**c**) *Z* axis

Figure 5. Representative environment vibrations for three axes of train cabin interior, including time domain vibration data and FFT analysis.

2.3. Stress Responses Used for Power Prediction

The aim of obtaining the stress responses in this section is used as input for power prediction. Apparently, the stresses on the half chassis structure varies with the time-dependent accelerations. For example, the displacements and von Mises stress responses under three axes accelerations randomly selected at 2.016 s are shown in Figure 6. The chassis behaves in lateral and bending mode under *Y* and *Z*-axis accelerations, respectively, with a maximum displacement of 2.43 mm and 14.23 mm at the middle of the chassis. Under *X*-axis acceleration, the chassis structure performs primarily in longitudinal bending deformation, with the nose structure deforming a maximum of 3.13 mm. Considering at the stress distributions under three axes, stress concentrates at the lower chassis connection points (red circle in Figure 6) and around the bogie mount central (yellow box in Figure 6). A larger stress can also be observed on the chassis beams when *Z*-axis acceleration is employed due to the bending deformation.

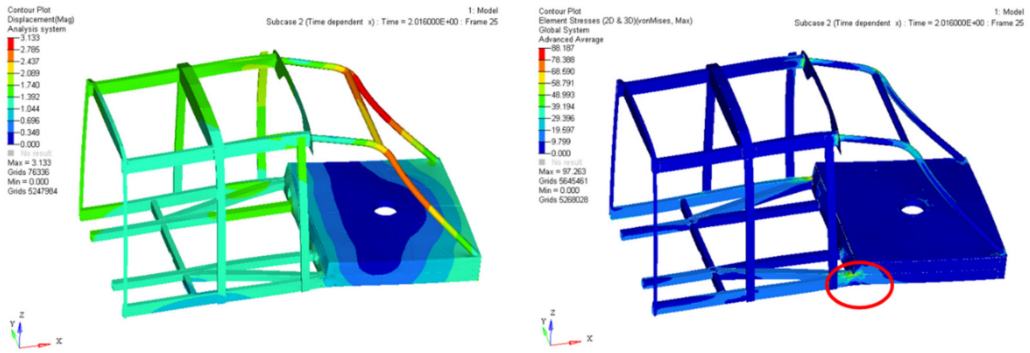

(**a**) Left side: displacement and right side: stress distributions under X axis acceleration

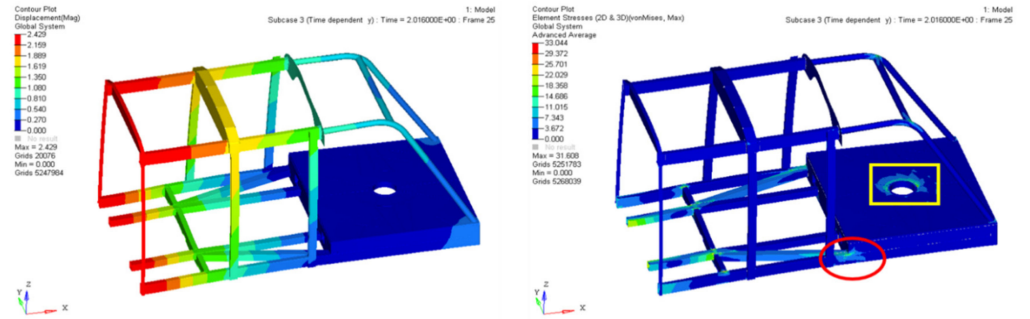

(**b**) Left side: displacement and right side: stress distributions under Y axis acceleration

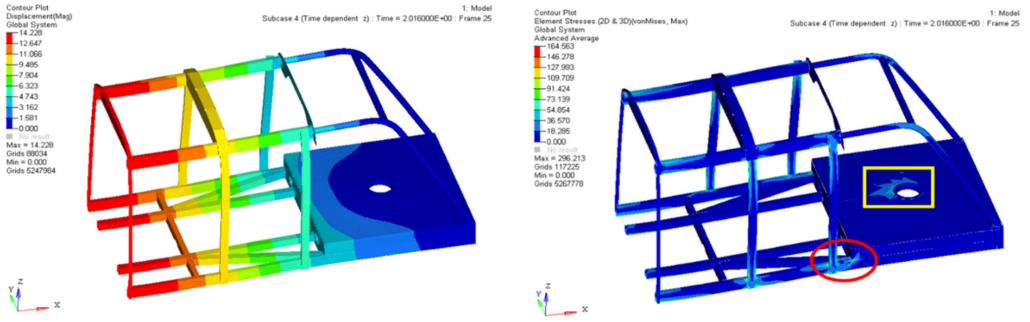

(**c**) Left side: displacement and right side: stress distributions under Z axis acceleration

Figure 6. Left side: displacement and right side: stress distributions of the half chassis model under (**a**) X-axis (Scale factor = 100), (**b**) Y-axis (Scale factor = 100) and (**c**) Z-axis (Scale factor = 50) accelerations at 2.016 s; red and yellow box circles the high stress regions at lower chassis connection and bogie mount, respectively.

Figure 7 indicates the relationship of von Mises stress vs. time of two elements located at the highest stressed lower chassis and bogie mount central. The signs of the stresses are defined in alignment with the directions of the displacements according to the local axes. The stresses at the two locations peak at approximately 100 MPa, which is much smaller than the tensile strength of the composite materials (662 MPa [32]). It can be seen that the vibration at the bogie mount fluctuates more than that at the lower chassis, indicating a less stable design.

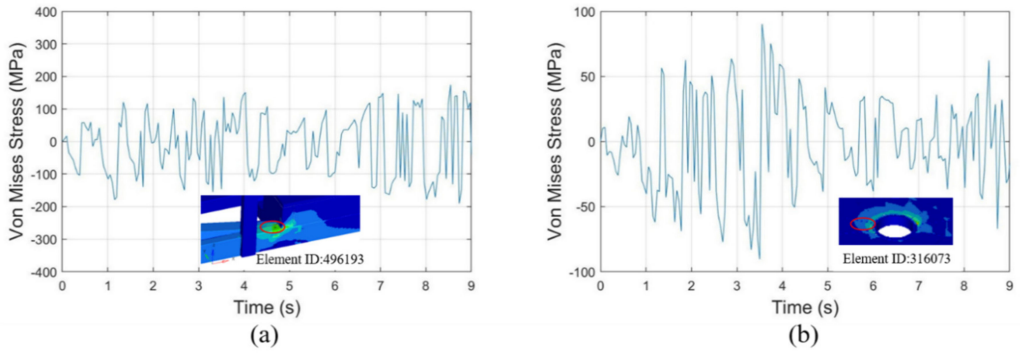

Figure 7. Von Mises stresses vs. time plots of (**a**) lower chassis connection, and (**b**) bogie mount central.

3. Power Generation and Management

3.1. AC Power Prediction Using MFC Piezoelectric Material

The embedded MFC-P2 transducers with designed shape of geometry and dimensions from [33] can be used as the energy harvester. The MFCs were modelled as orthotropic materials using the mechanical properties presented in Table 3, with E_x and E_y aligned to the rod and electrode directions, respectively. The piezoelectric and dielectric properties of the MFC are shown in Table 4. In accordance with the time-varying stress distributions in the chassis structure obtained from FE analysis considering the aim of harvesting the highest power, eight MFC location possibilities (as shown in Figure 8a,b) were evaluated which cover the stress concentration areas and high stress regions. MFC 1 to MFC 4 are designed in rectangular geometry of 100 × 50 × 0.3 mm^3 and MFC 5 (same as MFC 6) to MFC 7 (same as MFC 8) are designed in triangular shape with area domains of 13,488.2 mm^3 and 17,789.3 mm^3, to fit the geometry of the bogie mount structures. It should be noted that the acoustic impedance mismatch between the piezoelectric MFC and carbon fiber used in the simulation is ignored, as its effect is relatively low compared to the mechanical vibration and also the interested frequency in our application is lower compared to that of acoustic.

Table 3. Mechanical properties of MFC [33], E_x and E_y are the elastic modulus in the rod and electrode directions, respectively.

E_x (GPa)	E_y (GPa)	G_{xy} (GPa)	ν_{xy}	Density (kg/m^3)
30.34	15.86	5.52	0.31	5400

Table 4. Piezoelectric and dielectric properties of MFC [33].

Charge Constant d_{31} (pC/N)	−170
Charge constant d_{33} (pC/N)	400
Capacitance per unit area C_p (nF/cm2)	7.8
Dielectric permittivity ε_p	0.15

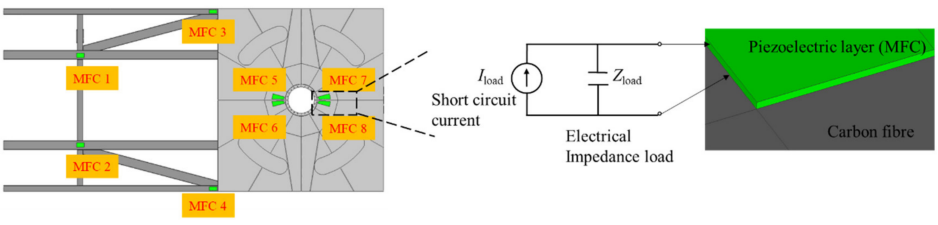

Figure 8. (**a**) The location possibilities of the MFC transducers on carbon fiber chassis structure, (**b**) the principle of the MFC transducer used to generate electrical power based on an electrical load, Z_{load}.

The time-varying stress responses from the MFC piezoelectric materials were calculated from the time dependent analysis of the global vehicle FE model. Typically, the MFC used in the chassis is ideally suited for vibration energy harvesting even in higher modes, as the opposing stress regions across the single MFC element which might result in partial charge cancellation have not been observed from the FE simulation. This is because the deformation in the MFC region is comparatively small and consistent compared to the large deformation of the entire vehicle. When used as an energy harvester, the piezoelectric material can work in d_{31} or d_{33} mode depending on the poling direction and the stress direction. It is typical that the d_{31} mode is usually seen in piezoelectric films, where the electric field is perpendicular to the direction of mechanical strain; the d_{33} mode appears as piezoelectric stacks where both electric field and strain are in the poling direction. As charge constant, d, is defined as the short circuit charge density per applied mechanical stress, the generated short circuit charge and current can be summarised by Equations (1) and (2) [29],

$$Q_{sc}(t) = d_{31}\sigma_{av}(t)\int_A dA \tag{1}$$

$$I_{sc}(t) = \omega(t)d_{31}\sigma_{av}(t)\int_A dA \tag{2}$$

where Q_{sc} is the short circuit electrical charge; I_{st} is the short circuit current; σ_{av} is the average stress experienced by the piezoelectric domain and A is the active area of the piezoelectric domain; ω is the frequency where the piezoelectric transducer excites, FFT was carried out on the time domain response from the FE simulation in order to assess the frequency characteristics.

For a given electrical impedance load Z_{load}, the current generated across the load, I_{load} (t) is given by Equation (3). To maximise power output, impedance matching is needed between Z_{load} and Z_i. For short circuit, $Z_{load} = 0$, the factor $\frac{Z_i}{\sqrt{Z_i^2+Z_{load}^2}} = 1$. As $Z_{load} \to \infty$, $\frac{Z_i}{\sqrt{Z_i^2+Z_{load}^2}} \to 0$. Therefore, the generated power across a matched impedance load, P_m can be calculated using the following Equations:

$$I_{load}(t) = \frac{I_{sc}(t)Z_i}{\sqrt{{Z_i}^2 + {Z_{load}}^2}} \tag{3}$$

$$Z_{load}(t) = Z_i(t) = \frac{1}{\omega(t)C_p} \tag{4}$$

$$P_m(t) = {I^2}_{load}(t)Z_{load} \tag{5}$$

where C_p is the capacitance of the piezoelectric material.

With the above-mentioned Equations (1)–(5), the power output from each MFC piezoelectric material as well as the total power output were calculated and plotted in Figure 9. The total mean power output from 8 MFCs is 28.34 mW, and the peak harvested power during the analysed time period exceeds 100 mW. However, this calculated power is unstable AC power, which is not suitable to transmit, store and distribute efficiently. For the purpose of a better conversion and management of the harvested energy, conditioned DC power is always adopted.

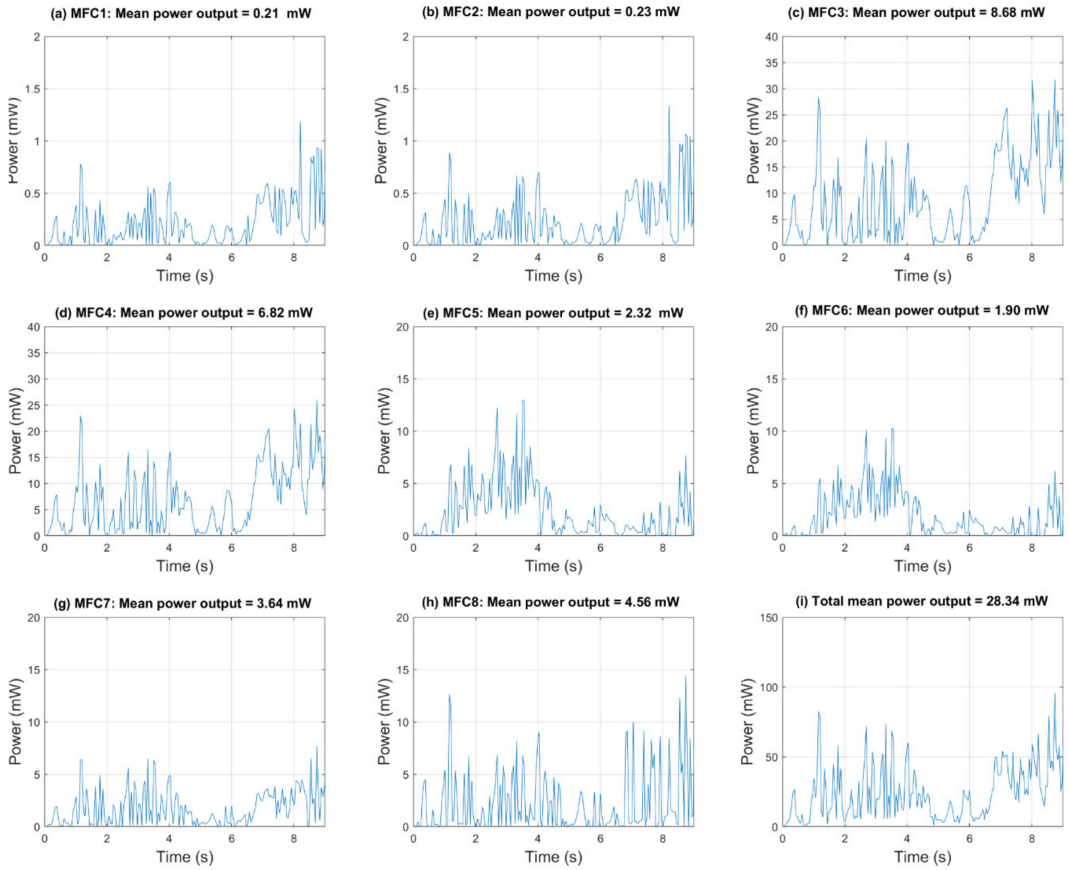

Figure 9. Power output calculated from 8 MFC piezoelectric materials.

3.2. Rectified Power Prediction

Since the harvested power is to be used to power electronic devices, which typically require DC power supplies, rectification circuits are needed to provide usable DC power for potential loads. This section provides the rectified output power estimation and analysis using both passive and popular active rectification circuits. Full-bridge rectifiers (FBR) are widely used due to simplicity and stability; however, the poor output power of FBRs has hindered the development of active rectification circuits in the past decade [34]. The synchronised switch harvesting (SSH) architecture is one of the most promising rectification systems to provide high energy efficiency for piezoelectric energy harvesting [35]. In this section, the output power from a passive FBR, switch-only (SO) and SSH on capacitors (SSHC) was simulated and analysed to show the peak DC output of the proposed energy harvesting system.

The circuit diagrams of an FBR, a SO rectifier and an SSHC rectifier are shown in Figure 10. The storage capacitors (C_S) used in the simulations were chosen at 1 mF. In the diagrams, the piezoelectric transducer (PT) has been modelled as a current source (I_P) in parallel with its inherent capacitor (C_P). In these three rectifiers, only the FBR is a passive rectifier using four passive diodes. The SO and SSHC rectifiers are active rectifiers requiring additional circuit designs to generate the control signals to drive the switches. The circuit implementations of the SSHC rectifier have been detailed in [35]. The number k represents the number of capacitor stages to perform as a k-stage SSHC rectifier. The SO rectifier is a simplified SSHC rectifier with the ϕ_0 switch only by removing all the following capacitor stages. Hence, the SO rectifier can be also regarded as a zero-stage SSHC rectifier.

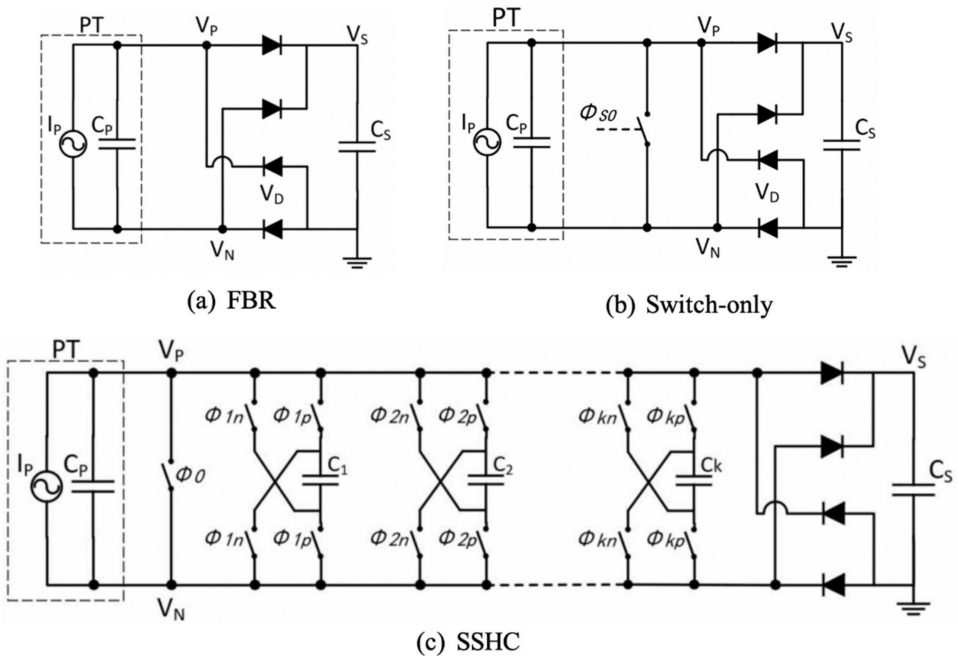

Figure 10. (**a**) Circuit diagram of an FBR, (**b**) a SO rectifier and (**c**) an SSHC rectifier.

The rectified output power of all eight MFC elements when using different rectification circuits was simulated and is shown in Figure 11. The simulations were based on the current sources calculated from the linear piezoelectric theory with the average stress outputs obtained from finite element analysis. The horizontal axis is the output voltage of the rectifier, which is also the voltage across the output capacitor connected at each rectification circuit, V_S, as shown in Figure 11. For the SSHC rectifier, different numbers of employed capacitors are simulated for various output power values with different performance levels. The more capacitors that are employed, the higher the peak output power that is achieved. However, more capacitors in SSHC rectifiers also result in more complicated control circuits, larger system sizes and higher optimal output voltage levels to achieve the peak power. The simulations were performed for V_S values ranging up to 300 V. The peak output power of each rectifier and the corresponding optimal output power are summarised in Table 5. From this table, it can be found that when using a passive FBR, the peak rectified power is around 21.2 mW from all eight MFC elements. When an eight-stage SSHC rectifier is employed, the peak rectified power achieves 181.9 mW, which is more than eight times higher compared to a passive FBR. In order to achieve this high output power, the output voltage, V_S, of the SSHC rectifier needs to be maintained at around 300 V. Since this optimal voltage is usually higher than the supply voltages for most low-power loads, an efficiency DC-DC converter and a voltage regulator are typically required to power the load electronics.

Table 5. Peak rectifier power for each rectification circuit and the corresponding optimal output voltage.

Rectifiers	Peak Power (mW)	Optimal V_S (V)
FBR	21.2	48
Switch-only	42.3	96
SSHC (1-cap)	63.4	144
SSHC (2-cap)	84.6	192
SSHC (4-cap)	126.9	288
SSHC (8-cap)	181.9	300

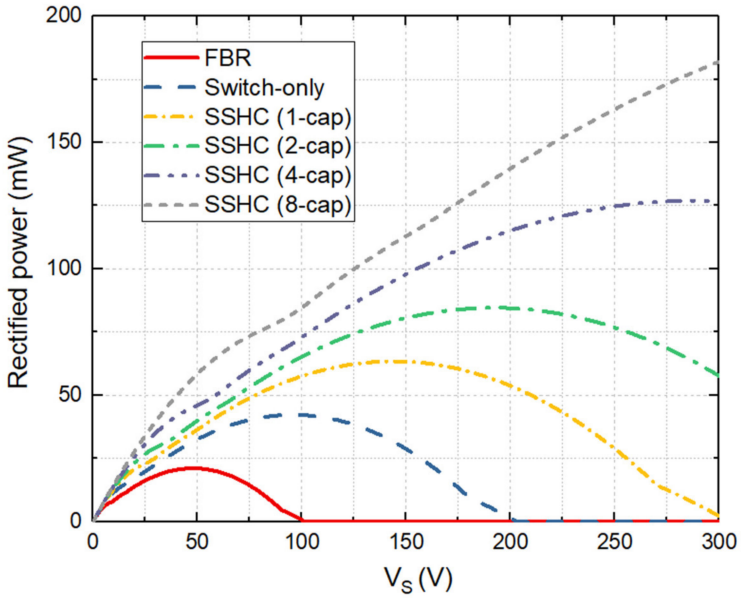

Figure 11. Simulated rectified output power using FBR, switch-only (SO) rectifier and SSHC rectifier (with different numbers of capacitor stages) for all the eight MFC elements.

It is worthwhile analysing the power contributions from different MFC elements for future design optimisations. The peak rectified output power values from individual MFC elements are shown in Table 6. It can be clearly seen that the MFC 3 and MFC 4 contribute more than 90% of the total rectified power. This is because MFC 3 and MFC 4 are mechanically located at stress concentration regions (welding connections within the adjacent host structures), inducing a high stress output and therefore the highest power output.

Table 6. Peak output power from individual MFC elements and their contributions to the total power.

	Peak Rectified Power (mW)						Percentage (%)
MFC No.	**FBR**	**Switch-only**	**SSHC (1-cap)**	**SSHC (2-cap)**	**SSHC (4-cap)**	**SSHC (8-cap)**	
1	0.28	0.56	0.84	1.12	1.68	2.79	**1.2**
2	0.31	0.61	0.92	1.23	1.84	3.06	**1.3**
3	11.89	23.78	35.67	47.57	71.35	118.92	**51.7**
4	9.34	18.68	28.01	37.35	56.03	93.38	**40.6**
5	0.24	0.47	0.71	0.94	1.41	2.36	**1.0**
6	0.19	0.39	0.58	0.77	1.16	1.94	**0.8**
7	0.35	0.69	1.04	1.38	2.07	3.46	**1.5**
8	0.41	0.82	1.22	1.63	2.45	4.08	**1.8**

4. Discussion on Use of Power Budget

It is clear that it is impossible for the energy harvesting from the vehicle vibration meet the power requirement of the motors and actuators itself, as the motive power requirement is more than an order of magnitude higher than what energy harvesting can provide. However, the recoverable power is sufficient to meet the power requirements of sensors, microprocessors and wireless systems which are important to railway infrastructures to regulate maintenance and to ensure safety. In order to study the impact of the recovered power, a possible route for the new rail vehicle was analysed. The vehicle speed based on initial route assumptions is shown in Figure 12. The route is defined over a route of 14 km within the City of Coventry, with known locations of seventeen stop stations. The route speed limit is defined according to the standards in the United Kingdom. The entire running time period of one route is approximately 20 min (1200 s) based on the speed limits.

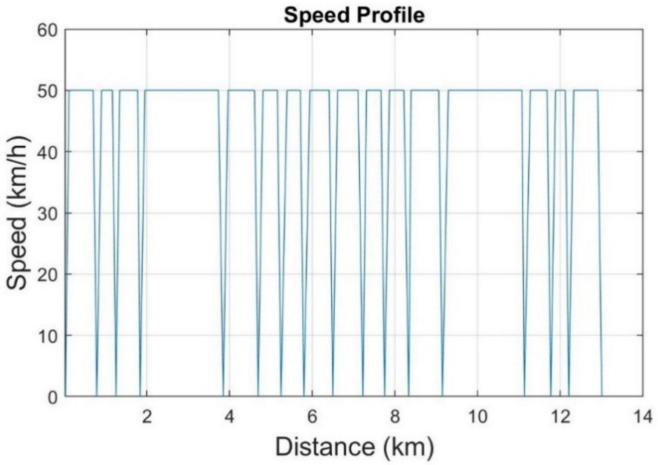

Figure 12. Speed profile of this vehicle vs. distance.

In order to assess the meaningfulness of the calculated recoverable power, the typical power requirements of various functional sensors, controllers and wireless systems are summarised in Table 7. Some of the power consumptions do not need to be in active operation all the time and smart power management can help to reduce the power budget. The power requirement for one journey was estimated to be 153 mW, and this could be met by the harvested power from the vehicle vibrations. Table 8 compares different types of rail harvesting sources from the open literature to evaluate the accuracy of the calculated power budget as well as to understand the harvested power contributions from a wide range of sources. Most of the literature investigated energy harvesting from train-induced railway track vibrations, such as Wang et al. [36] and Wang et al. [37], who proposed the use of an electromagnetic generator and piezoelectric transducers embedded in the track to harvest energy from the moving vehicle loads mainly via experimental testing. Cleante et al. [38] analytically investigated the amount of harvested energy induced by a passing train at various speeds using a trackside energy harvester. Tehrani et al. [39] analytically calculated a single spring-mass-damper system used as the energy harvester with the measured acceleration from a train cabin. Although these works contain basic analytical modelling, they lack consideration of sprung mass vibrations and the electronic network between various energy harvesters. Wheelwright et al. [40] established a vibration-based condition system product for the monitoring, management and maintenance of wheelsets of rolling stock to prevent failures. In terms of the railway station network, Jiang et al. [41] built electronics storage schemes for regenerative energy from railway stations to reduce the operating costs and improve the operational safety of railways. However, for the first time, this work takes account of energy harvesting from sprung mass vibrations in the train chassis using both finite element modelling of prototype design and electronics simulation optimisation, which is more representative of the realistic scenarios.

Table 7. Estimated power budget of the sensor platform with the application of the route assumption of this vehicle.

Power Budget Item	Power (mW)	Active in Period (%)	Active Time in One Route Cycle (s)	Power in One Route Cycle (mW)
MEMS 9 DOF motion sensor + MPU [42] × 2 units	0.05	100%	1200	1
Inclinometers [43] × 2 units	56.25	100%	1200	112.50
Distance sensors [44] × 2 units	13.95	100%	1200	27.90
Microprocessor unit (MPU) (active mode [45]) × 2 units	0.36	100%	1200	0.72
Bluetooth 5 + RF chip (transceiver mode [46]) × 2 units	27	20%	240	10.80
Bluetooth 5 + RF chip (sleep mode, clock [46]) × 2 units	0.045	80%	960	0.08
	Sum			**153.00**

Table 8. Different types of energy harvested in the rail from the literature.

Type of Rail Harvesting	Energy Harvest	Methodology	Comments
Train induced track vibration	2–4 V	Experiments	For 6.35 mm track displacement input, from Wang et al. [36]
	0.02–0.2 mW	Experiments Analytical modelling	For slack-type and patch-type piezoelectric transducers, from Wang et al. [37]
	100.3–157.1 mW	Analytical modelling	With passing train speed from 190 to 200 km/h, from Cleante et al. [38]
Electrification of railway stations	541.6 kW	Electronics simulation	Jiang et al. [41]
Unsprung mass vibration	21.4 mW	Analytical modelling	Ghandchi Tehrani et al. [39]
	1–5 wheel health index	Experiments	Wheelwright et al. [40]
Sprung mass vibration	21.2–181.9 mW	Finite element modelling Electronics simulation	This work

5. Conclusions

This paper presented the energy generation from a multifunctional MFC-embedded composite chassis of a rail structure. The rectification circuits are designed to help the optimisation and power management for harvested energy under the real-world vibration data measured in a cabin of a rail vehicle. A finite element model was built to numerically predict the time dependent stress responses using representative three axis acceleration data. Eight locations were therefore determined at the bottom chassis for integrating the piezoelectric energy harvesters. The analytical model was developed to explain the energy harvesting mechanisms. The rectification circuit design of the various passive and active rectification systems was proposed to help the optimisation and management of harvested energy. The results showed that a peak of 181.9 mW DC electric power was approximately recovered when an eight-stage SSHC rectifier was employed. Compared to the other designs and case without such circuit design optimisation, it generates high output power compared to the AC power, FBR and the switch-only rectifier which makes it suitable to meet the required power budget. The power level achieved by harvesting operational vibration was considered to be sufficiently and continuously sustain a simple sensor service platform, considering a hypothetical average power budget consumption of 153 mW. The novel optimisation using rectification circuits for improving the efficiency of energy harvesting has rarely been reported and the success of maximising the energy harvested in this paper

offers a significant opportunity to enable micro-watt power scavenging from ambient vibrations towards the realistic applications.

In the near future, a prototype of the composite chassis of the rail vehicle will be fabricated with integration of energy harvesters based on the current design, nonlinear vibration spectrum [47] and optimised rectification circuits. Experimental testing under mechanical vibrations with the various operational and environmental conditions will be performed to validate this work, which will carve a route for further exploitation—not only in the rail industry, but also the automotive, offshore wind energy and aerospace sectors.

Author Contributions: Conceptualization, Y.L., S.D., Y.J. and Y.S.; Data curation, Y.L., S.D. and Y.J.; Methodology, Y.L., S.D., Y.J. and Y.S.; Software, Y.L. and S.D.; Validation, Y.J., Y.S., and D.J.H.; Writing-review and editing, Y.L., S.D., C.M., Y.J. and Y.S and D.J.H.; Visualization, C.M., Y.J., Y.S., and D.J.H.; Supervision, Y.J., Y.S., and D.J.H. All authors have read and agreed to the published version of the manuscript.

Funding: This research received no external funding.

Acknowledgments: This work was supported under the Coventry Light Rail Project at WMG, University of Warwick, supported by Coventry City Council and the West Midlands Combined Authority. The vehicle structure was designed in collaboration with TDI Ltd., UK.

Conflicts of Interest: The authors declare no conflict of interest.

Abbreviations

The following abbreviations are used in this manuscript:

CFRP	carbon fiber reinforced polymer
FBR	full-bridge rectifiers
FEA	finite element analysis
MFC	micro fiber composites
SO	switch-only
SSHC	synchronized switch harvesting capacitors

References

1. Zuo, L.; Tang, X. Large-scale vibration energy harvesting. *J. Intell. Mater. Syst. Struct.* **2013**, *24*, 1405–1430. [CrossRef]
2. Zuo, L.; Scully, B.; Shestani, J.; Zhou, Y. Design and characterization of an electromagnetic energy harvester for vehicle suspensions. *Smart Mater. Struct.* **2010**, *19*, 45003. [CrossRef]
3. Glynne-Jones, P.; Tudor, J.; Beeby, S.P.; White, N. An electromagnetic, vibration-powered generator for intelligent sensor systems. *Sens. Actuators A Phys.* **2004**, *110*, 344–349. [CrossRef]
4. Erturk, A.; Inman, D.J. *A Brief Review of the Literature of Piezoelectric Energy Harvesting Circuits*; Wiley: Hoboken, NJ, USA, 2011.
5. Lu, Q.; Liu, L.; Scarpa, F.; Leng, J.; Liu, Y. A novel composite multi-layer piezoelectric energy harvester. *Compos. Struct.* **2018**, *201*, 121–130. [CrossRef]
6. Jia, Y.; Yan, J.; Soga, K.; Seshia, A.A. Parametrically excited MEMS vibration energy harvesters with design approaches to overcome the initiation threshold amplitude. *J. Micromech. Microeng.* **2013**, *23*, 114007. [CrossRef]
7. Zhu, G.; Chen, J.; Liu, Y.; Bai, P.; Zhou, Y.; Jing, Q.; Pan, C.; Wang, Z.L. Linear-Grating Triboelectric Generator Based on Sliding Electrification. *Nano Lett.* **2013**, *13*, 2282–2289. [CrossRef]
8. Zhu, G.; Lin, Z.-H.; Jing, Q.; Bai, P.; Pan, C.; Yang, Y.; Zhou, Y.; Wang, Z.L. Toward Large-Scale Energy Harvesting by a Nanoparticle-Enhanced Triboelectric Nanogenerator. *Nano Lett.* **2013**, *13*, 847–853. [CrossRef]
9. Lafont, T.; Gimeno, L.; Delamare, J.; A Lebedev, G.; I Zakharov, D.; Viala, B.; Cugat, O.; Galopin, N.; Garbuio, L.; Geoffroy, O. Magnetostrictive–piezoelectric composite structures for energy harvesting. *J. Micromech. Microeng.* **2012**, *22*, 94009. [CrossRef]

10. Minsili, L.S.; Xia, H.; Eko, R.M. Analytical model of underground train induced vibrations on nearby building structures in Cameroon: Assessment and prediction. *Leonardo Electron. J. Pract. Technol.* **2013**, *12*, 63–82.
11. Gill, K.S. Cognitive Radio Connectivity for Railwa Transportation Networkds. Master's Thesis, Worcester Polytechnic Institute, Worcester, MA, USA, 2018.
12. Tao, K.; Lye, S.W.; Miao, J.M.; Hu, X.M. Performance enhancement of an out-of-plane electret-based vibrational energy harvester with dual charged plates. *J. Phys. Conf. Ser.* **2014**, *557*, 012064. [CrossRef]
13. Li, H.; Tian, C.; Deng, Z.D. Energy harvesting from low frequency applications using piezoelectric materials. *Appl. Phys. Rev.* **2014**, *1*, 041301. [CrossRef]
14. Dai, H.L.; Abdelkefi, A.; Javed, U.; Wang, L. Modeling and performance of electromagnetic energy harvesting from galloping oscillations. *Smart Mater. Struct.* **2015**, *24*, 45012. [CrossRef]
15. Gao, M.; Wang, P.; Cao, Y.; Chen, R.; Cai, D. Design and Verification of a Rail-Borne Energy Harvester for Powering Wireless Sensor Networks in the Railway Industry. *IEEE Trans. Intell. Transp. Syst.* **2016**, *18*, 1–14. [CrossRef]
16. Al-Saadi, A.; Shi, Y.; Pan, L.; Tao, J.; Jia, Y. Vibration energy harvesting of multifunctional carbon fibre composite laminate structures. *Compos. Sci. Technol.* **2019**, *178*, 1–10. [CrossRef]
17. Beeby, S.P.; Tudor, M.J.; White, N. Energy harvesting vibration sources for microsystems applications. *Meas. Sci. Technol.* **2006**, *17*, R175–R195. [CrossRef]
18. Chen, J.; Wang, Z.L. Reviving Vibration Energy Harvesting and Self-Powered Sensing by a Triboelectric Nanogenerator. *Joule* **2017**, *1*, 480–521. [CrossRef]
19. Sosnicki, O.; Lhermet, N.; Claeyssen, F. Vibration energy harvesting in aircraft using piezoelectric actuators. *Proc. Actuator* **2006**, *21*, 968–971.
20. Shi, Y.; Hallett, S.; Zhu, M. Energy harvesting behaviour for aircraft composites structures using macro-fibre composite: Part I—Integration and experiment. *Compos. Struct.* **2017**, *160*, 1279–1286. [CrossRef]
21. Tianchen, Y.; Jian, Y.; RuiGang, S.; Xiaowei, L. Vibration energy harvesting system for railroad safety based on running vehicles. *Smart Mater. Struct.* **2014**, *23*, 125046. [CrossRef]
22. Pourghodrat, A.; Nelson, C.A.; E Hansen, S.; Kamarajugadda, V.; Platt, S.R. Power harvesting systems design for railroad safety. *Proc. Inst. Mech. Eng. Part F J. Rail Rapid Transit* **2013**, *228*, 504–521. [CrossRef]
23. Hadas, Z.; Smilek, J.; Rubes, O. Energy harvesting from passing train as source of energy for autonomous trackside objects. *MATEC Web Conf.* **2018**, *211*, 05003. [CrossRef]
24. Du, S.; Jia, Y.; Arroyo, E.; Fernandez, S.; Riches, S.T.; Seshia, A.A. MEMS Piezoelectric Energy Harvester Powered Wireless Sensor Module Driven by Noisy Base Excitation. In Proceedings of the 2019 20th International Conference on Solid-State Sensors, Actuators and Microsystems & Eurosensors XXXIII (TRANSDUCERS & EUROSENSORS XXXIII), Berlin, Germany, 23–27 June 2019; pp. 350–353.
25. Jia, Y.; Yan, J.; Du, S.; Feng, T.; Fidler, P.; Middleton, C.; Soga, K.; Seshia, A.A. Real world assessment of an auto-parametric electromagnetic vibration energy harvester. *J. Intell. Mater. Syst. Struct.* **2017**, *29*, 1481–1499. [CrossRef]
26. Du, S.; Jia, Y.; Zhao, C.; Chen, S.-T.; Seshia, A.A. Real-world evaluation of a self-startup SSHI rectifier for piezoelectric vibration energy harvesting. *Sens. Actuators A Phys.* **2017**, *264*, 180–187. [CrossRef]
27. Erturk, A.; Inman, D.J. An experimentally validated bimorph cantilever model for piezoelectric energy harvesting from base excitations. *Smart Mater. Struct.* **2009**, *18*, 25009. [CrossRef]
28. Erturk, A.; Inman, D.J. A Distributed Parameter Electromechanical Model for Cantilevered Piezoelectric Energy Harvesters. *J. Vib. Acoust.* **2008**, *130*, 041002. [CrossRef]
29. Jia, Y.; Wei, X.; Xu, L.; Wang, C.; Lian, P.; Xue, S.; Al-Saadi, A.; Shi, Y. Multiphysics vibration FE model of piezoelectric macro fibre composite on carbon fibre composite structures. *Compos. Part B Eng.* **2019**, *161*, 376–385. [CrossRef]
30. Winnett, J.; Hoffrichter, A.; Iraklis, A.; McGordon, A.; Hughes, D.J.; Ridler, T.; Mallinson, N. Development of a very light rail vehicle. *Proc. Inst. Civ. Eng. Transp.* **2017**, *170*, 231–242. [CrossRef]
31. Gulf Coast Data Concepts. X16-1D USB MEMS Accelerometer Data Loggers. 2016. Available online: http://www.gcdataconcepts.com/xlr8r-1.html (accessed on 25 May 2020).
32. Prepreg Fabric—GURIT SE84LV/RC200T/42%. Available online: https://www.900gpa.com/en/product/prepregCompound/FabPreg_00FABBBA10?u=metric (accessed on 16 October 2019).
33. Microfibre Composites (MFC) P2, P3 Type. Smart Compos n.d. Available online: https://www.smart-material.com/MFC-product-P2.html (accessed on 15 October 2019).

34. Du, S.; Jia, Y.; Zhao, C.; Amaratunga, G.A.J.; Seshia, A.A. A Passive Design Scheme to Increase the Rectified Power of Piezoelectric Energy Harvesters. *IEEE Trans. Ind. Electron.* **2018**, *65*, 7095–7105. [CrossRef]
35. Du, S.; Jia, Y.; Zhao, C.; Amaratunga, G.A.J.; Seshia, A.A. A Fully Integrated Split-Electrode SSHC Rectifier for Piezoelectric Energy Harvesting. *IEEE J. Solid-State Circuits* **2019**, *54*, 1733–1743. [CrossRef]
36. Wang, J.J.; Penamalli, G.P.; Zuo, L. Electromagnetic energy harvesting from train induced railway track vibrations. In Proceedings of the 2012 IEEE/ASME 8th IEEE/ASME International Conference on Mechatronic and Embedded Systems and Applications, Suzhou, China, 8–10 July 2012; Volume 11787, pp. 29–34. [CrossRef]
37. Wang, J.; Shi, Z.; Xiang, H.-J.; Song, G. Modeling on energy harvesting from a railway system using piezoelectric transducers. *Smart Mater. Struct.* **2015**, *24*, 105017. [CrossRef]
38. Cleante, V.G.; Brennan, M.J.; Gatti, G.; Thompson, D.J. Energy harvesting from the vibrations of a passing train: Effect of speed variability. *J. Phys. Conf. Ser.* **2016**, *744*, 12080. [CrossRef]
39. Tehrani, M.G.; Gatti, G.; Brennan, M.J.; Thompson, D.J.; Oscillator, L. Energy harvesting from train vibrations. In Proceedings of the 11th International Conference on Vibration Problems, Lisbon, Portugal, 8–11 September 2013; pp. 9–12.
40. Wheelwright, H.E.; Vincent, D. Track defect and wheel damage: Detection and location. *Perpetuum* Ltd. Available online: https://perpetuum.com/download/track-defect-and-wheel-damage-detection-and-location (accessed on 25 May 2020).
41. Jiang, B.Y.; Liu, J.; Tian, W.; Shahidehpour, M.; Krishnamurthy, M. Energy harvesting for the electrification of railway stations. *IEEE Electrif. Mag.* **2014**, *2*, 39–48. [CrossRef]
42. TDK-InvenSense. MPU-9250 Nine-Axis (Gyro + Accelerom + Compass) MEMS Motion Trackin Device n.d. Available online: https://www.invensense.com/products/motion-tracking/9-axis/mpu-9250/ (accessed on 25 October 2019).
43. SCA100T Inclinometers | Inclinometers | Sensors | Murata Manufacturing Co., Ltd. Available online: https://www.murata.com/en-sg/products/sensor/inclinometer/sca100t (accessed on 23 October 2019).
44. SRF08 Ultrasonic Sensor n.d. Available online: https://www.active-robots.com/srf08-ultrasonic-sensor.html (accessed on 23 October 2019).
45. STM32L4-ARM Cortex-M4 ultra-low-power MCUs-STMicroelectronics. Available online: https://www.st.com/en/microcontrollers-microprocessors/stm32l4-series.html (accessed on 23 October 2019).
46. Darroudi, S.M.; Caldera-Sànchez, R.; Gomez, C. Bluetooth Mesh Energy Consumption: A Model. *Sensors* **2019**, *19*, 1238. [CrossRef] [PubMed]
47. Jia, Y. Review of nonlinear vibration energy harvesting: Duffing, bistability, parametric, stochastic and others. *J. Intell. Mater. Syst. Struct.* **2020**, *31*, 921–944. [CrossRef]